

pubs.acs.org/journal/apchd5 Article

# Non-Line-of-Sight Detection Based on Neuromorphic Time-of-Flight Sensing

Minseong Park, Yuan Yuan, Yongmin Baek, Byungjoon Bae, Bo-In Park, Young Hoon Kim, Nicholas Lin, Junseok Heo,\* and Kyusang Lee\*



Cite This: ACS Photonics 2023, 10, 2739-2745

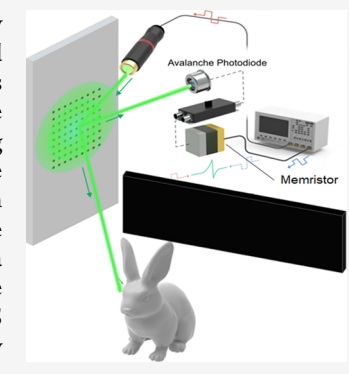


ACCESS

III Metrics & More

Article Recommendations

ABSTRACT: Non-line-of-sight (NLOS) detection and ranging aim to identify hidden objects by sensing indirect light reflections. Although numerous computational methods have been proposed for NLOS detection and imaging, the post-signal processing required by peripheral circuits remains complex. One possible solution for simplifying NLOS detection and ranging involves the use of neuromorphic devices, such as memristors, which have intrinsic resistive-switching capabilities and can store spatiotemporal information. In this study, we employed the memristive spike-timing-dependent plasticity learning rule to program the time-of-flight (ToF) depth information directly into a memristor medium. By coupling the transmitted signal from the source with the photocurrent from the target object into a single memristor unit, we were able to induce a tunable programming pulse based on the time interval between the two signals that were superimposed. Here, this neuromorphic ToF principle is employed to detect and range NLOS objects without requiring complex peripheral circuitry to process raw signals. We experimentally demonstrated the effectiveness of the neuromorphic ToF principle by integrating a HfO<sub>2</sub>



memristor and an avalanche photodiode to detect NLOS objects in multiple directions. This technology has potential applications in various fields, such as automotive navigation, machine learning, and biomedical engineering.

**KEYWORDS:** memristors, time-of-flight, avalanche photodiodes, non-line-of-sight, spike-timing-dependent plasticity, neuromorphic computing

# ■ INTRODUCTION

Mammalian visual systems employ a process known as spike-timing-dependent plasticity (STDP) that modulates synaptic weights based on the timing of presynaptic and postsynaptic spikes. The STDP learning rule is an asymmetrical and temporal form of Hebbian learning that facilitates sparse asynchronous spiking dynamics of synapses with low-power neurotransmissions. This process has been replicated in various artificial synaptic devices, such as resistive-switching random-access memories (ReRAMs), ferroelectric field-effect transistors, Mott transistors, and electrolyte-gated FETs. Among these, ReRAM exhibits nonvolatile resistive transitions based on both the timing and amplitudes of the applied electrical spikes, with the information stored as conductance.

In this study, we employed a memristive STDP learning rule to acquire non-line-of-sight (NLOS) information using the neuromorphic time-of-flight (ToF) principle. The ToF principle calculates the distance by measuring the time difference between the transmitted and received signals, considering the constant speed of light. The neuromorphic 3D sensing method is based on the ToF principle, which utilizes the overlap of the transmitted and received signals as the input for the memristor. Similar to the STDP learning rule, the conductance of the memristor is programmed using

temporal ToF information.  $^{10-12}$  This method facilitates the storage of the detected ToF information in a physical medium as conductance without requiring complex digital ToF architectures with numerous transistors and capacitors, resulting in a miniaturized system footprint. The neuromorphic 3D sensing also allows for a low power consumption of 0.171 mW for single depth acquisition,  $^{10}$  which is below the average power consumption of other conventional ToF architectures (0.1-0.65 mW) such as a vernier delay line,  $^{13}$  multiphase delay line,  $^{14}$  ring oscillator,  $^{15}$  and vernier ring oscillator.  $^{16}$ 

NLOS ranging is a promising 3D imaging application based on the ToF principle, which detects indirect optical signals for visualizing hidden objects. <sup>16</sup> To demonstrate a neuromorphic ToF system for NLOS sensing, we integrated the HfO<sub>2</sub> memristors with avalanche photodiodes and a laser light source, as shown in Figure 1a (for more details, see Methods). The flexible polyimide substrate allows the device to conform

Received: April 4, 2023 Published: June 13, 2023





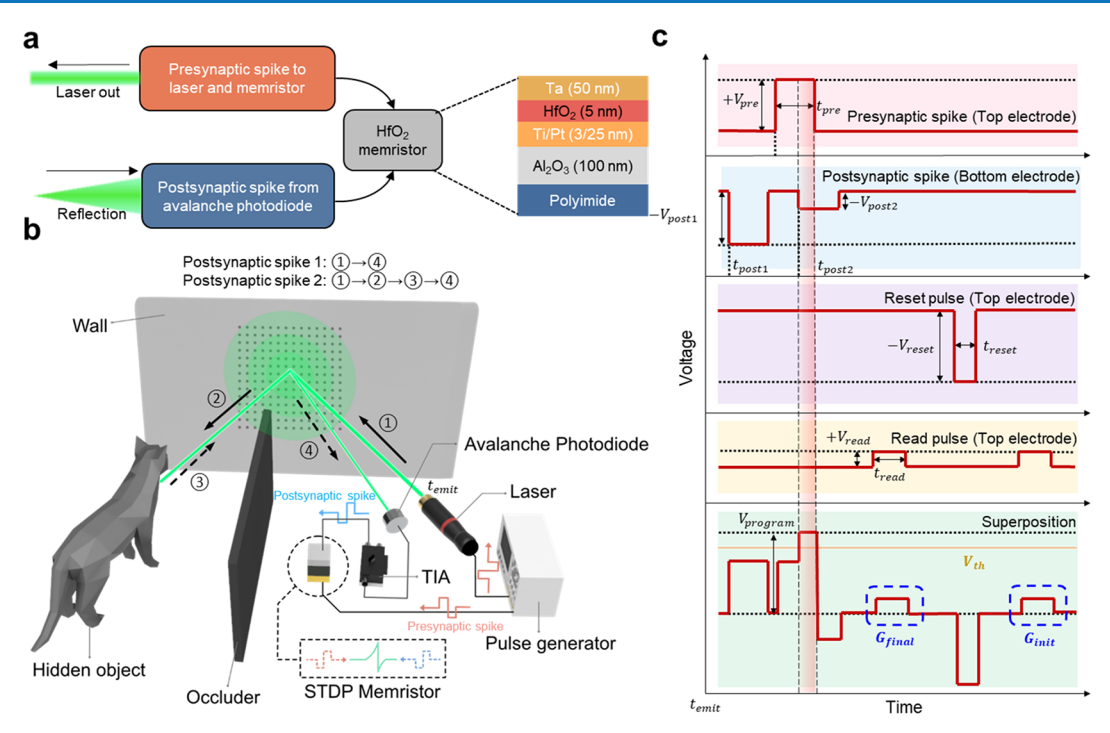


Figure 1. Neuromorphic NLOS detection. (a) Schematic of neuromorphic NLOS detection system. The  $HfO_2$  memristor stores the NLOS information as conductance via STDP. (b) Illustration of experimental neuromorphic NLOS detection setup. The presynaptic spike is generated via pulse generator, branched to both memristor and laser. The postsynaptic spike is converted from the reflected optical signal via the avalanche photodiode and the following transimpedance amplifier. The two spikes sandwich the memristor and program the memristor only if a target object is scanned. (c) Schematic waveforms of presynaptic and postsynaptic spikes, reset/read and super-positioned pulse signals to memristor from top to bottom for neuromorphic NLOS detection. The postsynaptic spike 2 is generated from the light scattered by the target object and is coupled with the presynaptic spike. The superposed waveform programs the memristor with a superposition peak higher than  $V_{\rm th}$ . Two read pulses are applied to the memristor to achieve  $G_{\rm final}$  and  $G_{\rm init}$ . The memristor conductance is initialized by the negative reset pulse.

to a variety of surfaces, enabling their potential use in widefield-of-view NLOS detection. Figure 1b illustrates the NLOS detection process using the neuromorphic ToF system. An electrical signal from a pulse generator was applied to both the memristor and a picosecond laser, which served as the presynaptic spike for the system (Alphalas PLDD-50M, 750 mW peak power). The emitted laser pulse was reflected off the target object and received by an avalanche photodiode (APD), which converted the signal into an electric current (Hamamatsu S9073). To detect NLOS objects, the emitted laser pulse first hits a reflective wall and partially scatters. The partially scattered rays then reach the hidden object. Subsequently, both the rays reflected from the wall and the hidden object reach the APD sequentially with respect to the distances of the ray propagations. The resulting signals are usually weak because of multiple reflections. Thus, the observed current signal is amplified and converted into a voltage signal (postsynaptic spike) using a tunable transimpedance amplifier (Edmund 59-179). In the neuromorphic ToF system, the input signal generated by the superposition of the presynaptic and postsynaptic spikes, referred to as a STDP learning rule, is used to program the depth information as the conductance of the memristor connected to the avalanche photodiode.

Figure 1c shows the waveform details of each spike and pulse in the neuromorphic ToF system. The observed information is converted into a postsynaptic spike that generates a superposed spike  $(V_{\rm program})$  capable of programming the connected memristor upon exceeding a threshold voltage  $(V_{\rm th})$ . Presynaptic and postsynaptic spikes were applied

to the top and bottom electrodes of the memristor, respectively. Therefore, the programming signal applied to the memristor is the potential difference between the positive presynaptic and negative postsynaptic spikes. The first postsynaptic spike originated from the rays that were directly reflected from the wall. Thus, the first postsynaptic spike did not contain information from the target object and was not coupled to the presynaptic spike. The first read pulse ( $V_{read}$  = 0.1 V and  $t_{\text{read}} = 10 \ \mu\text{s}$ ), after the neuromorphic ToF learning process, provides a programmed conductance  $(G_{\text{final}})$ . The programmed conductance is initialized by applying a reset pulse ( $V_{\text{reset}} = -1.5 \text{ V}$  and  $t_{\text{reset}} = 10 \,\mu\text{s}$ ) and then confirmed by the second read pulse  $(G_{initial})$ . The conductance transition is calculated as  $\Delta G = \frac{(G_{\rm final} - G_{\rm init})}{G_{\rm init}} \times 100(\%)$ . All the pulses were applied to the top electrode of the memristor, except for the postsynaptic spike.

Figure 2a shows the current–voltage (I-V) characteristics of the HfO<sub>2</sub> memristors, which were measured using a semiconductor analyzer (Keysight B1500A). Upon applying a set voltage of 1.5 V, the positive electric field induced a robust conductive bridge (made up of oxygen vacancies) within the memristor medium, causing the resistance of the memristor to abruptly transition from high to low. To prevent Joule heating degradation, the measurement setup included a 1 mA current compliance. When -1.5 V is applied to the memristor, the conductive bridge diminishes, causing the low-resistance state of the memristor to switch back to the high-resistance state (HRS). Figure 2b shows the pulse train of a memristor for analog resistance transition, which is a crucial property for

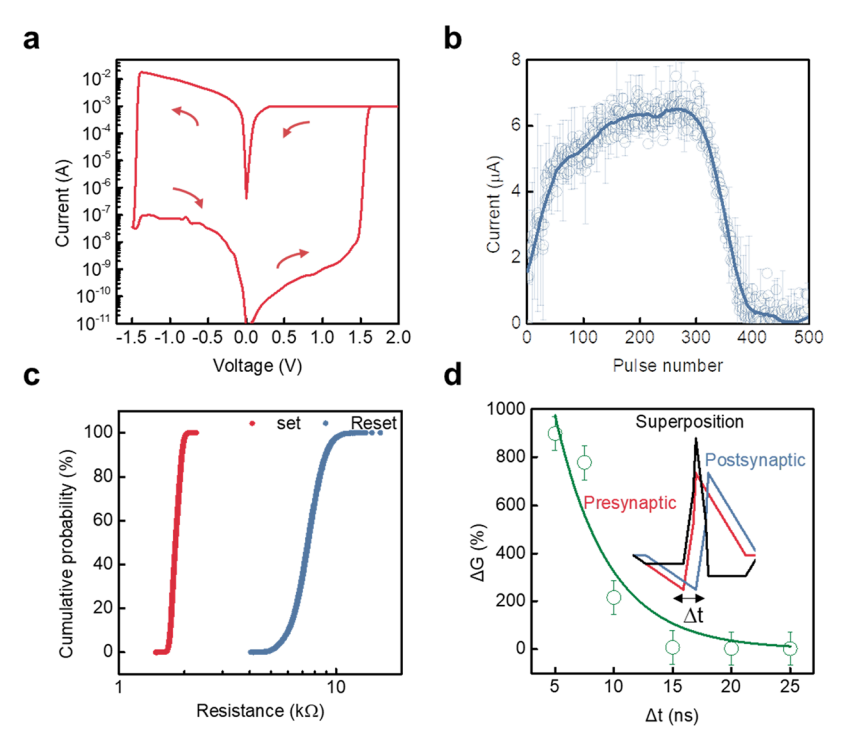
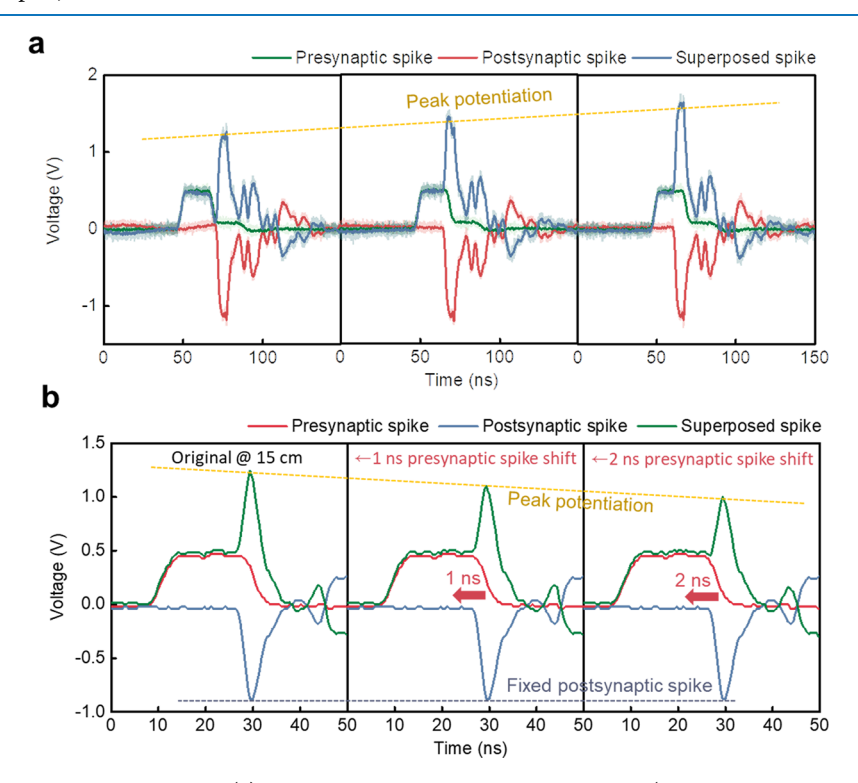
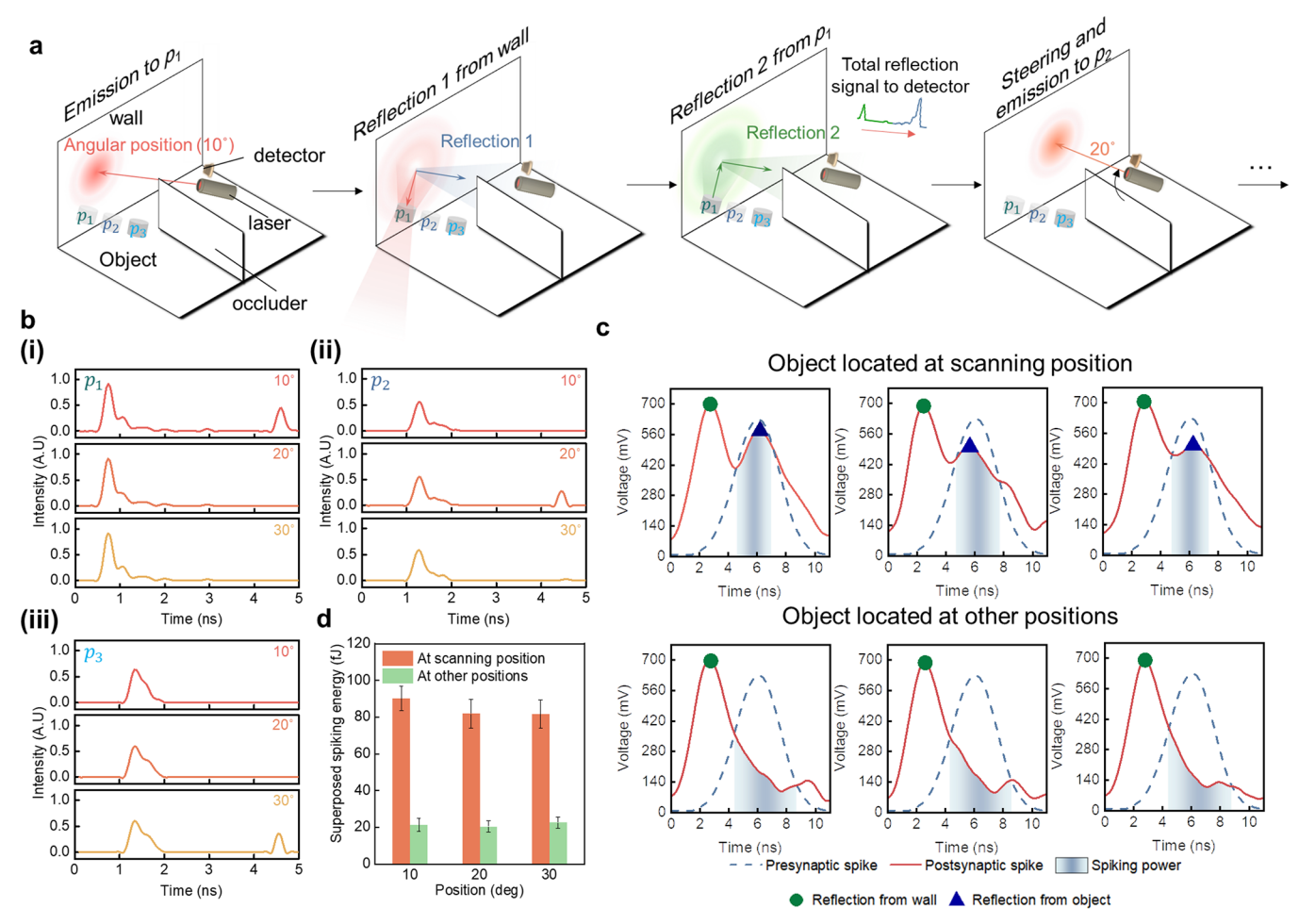


Figure 2. Electrical characteristics of artificial synapses. (a) DC current–voltage (I-V) characteristics of HfO<sub>2</sub> memristors. The set and reset voltages are approximately 1.5 and -1.5 V, respectively. The forming process was conducted at 4 V before the measurement. (b) Average and standard deviation of 250 pulses potentiation/250 pulses depression five-cycle conductance updates under incremental pulse conditions (200 ns pulse train with amplitudes from 0.8 to 1.2 V for potentiation and from -0.7 to -0.9 V for depression. (c) Cumulative probability plot of set and reset states for 100,000 cycles. The applied set and reset voltages are 1.5 and -2 V, respectively (20- $\mu$ s pulse). (d) Spike-timing dependent plasticity (STDP) response of HfO<sub>2</sub> memristors. Identical spike geometry is applied for both presynaptic and postsynaptic spikes (from -0.5 to 1.2 V with 20-ns peak-to-peak spike).



**Figure 3.** Neuromorphic ToF ranging waveforms. (a) STDP waveforms from the ToF ranging (40, 25, and 10 cm object distances from left to right). Light-color lines: before the smoothing process. (b) STDP waveforms from ToF ranging with fixed postsynaptic spike. The spike timing of the presynaptic spike is manually delayed with the fixed postsynaptic spike. The amplitude of the peak potentiation increases with the delay times that correspond to farther distance (30 and 45 cm).



**Figure 4.** Neuromorphic NLOS detection. (a) Schematic illustration of NLOS situation. The laser beam with one angular position  $(10^\circ, 20^\circ)$ , or  $30^\circ$ ) reaches the wall, partially reflected to the laser (Reflection 1). The propagating beam is also reflected from the hidden object  $(p_1, p_2, \text{ or } p_3)$  and then from the wall (Reflection 2). Both reflection signals are detected by the ToF sensor, and the laser steers the angle to another angular position for the next scanning. (b) Ray-tracing simulations of the NLOS detection. The first peak is from the direct reflection from the wall, and the second smaller peak is from the NLOS object when the object is located at positions  $p_1$  (i),  $p_2$  (ii), and  $p_3$  (iii). (c) Experimental results of the NLOS detection. The second peak is coupled to the electrical presynaptic spike to generate the STDP programming (top). Results without coupling for objects located at each  $p_1$ ,  $p_2$ , and  $p_3$  (bottom). (d) Experimental comparison of superposed spiking energy between the scanning positions. As the object is located at the nonscanning points, less coupling leads to less conductance switching of the memristor. The error bars indicate the standard deviation.

neuromorphic processing applications. We applied a pulse train of 200 ns with incremental amplitudes ranging from 0.8 to 1.2 V for potentiation (P) and decremental amplitudes ranging from -0.7 to -0.9 V for depression (D). A total of 250 potentiation pulses and 250 depression pulses were employed in a single-cycle test for the conductance update process, and this analog programming capability was utilized in neuromorphic ToF ranging to obtain the depth information.

We also studied the endurance of the resistive switching devices. The cumulative probability for 100,000 cycles of the set/reset operation of the memristors is presented in Figure 2c. The average resistances of each set and reset state are 1.815 and 7.287 k $\Omega$ , respectively. The resistance distribution of each state during the repeating cycles exhibits a Gaussian distribution with small set/reset variances (86.71 and 1.118 k $\Omega$ , respectively). The consistent resistive endurance of the memristor has potential applications in 3D imaging techniques, such as light detection and ranging (LiDAR). These techniques require the acquisition of massive point-by-point data through repeated emitting and receiving of optical flux.

We utilized the above-mentioned analog switching capability and high endurance of memristors to emulate the biological spike-timing-dependent plasticity learning rule for neuromorphic ToF ranging and NLOS detection applications. Figure 2d demonstrates the emulation of the STDP learning rule using memristors. Presynaptic and postsynaptic spikes were applied to the top and bottom electrodes of the memristors, respectively. Depending on the time difference between the two spikes, various amplitudes of superposed peaks can be achieved. These superposed peaks incorporate the presynaptic and postsynaptic spikes, programming the memristor. The conductance transition ( $\Delta G$ ) of the memristor increases when the spike-timing difference  $(\Delta t)$  is small. This increase can be interpreted as a short distance between the neuromorphic ToF system and a target object. We mathematically fit the relationship between conductance transition and distance as  $\Delta G = Ae^{-\Delta t/B}$ , where A and B are fitting parameters. This, combining with the ToF equation, enables the conductance-to-distance conversion to be achieved as a neuromorphic ToF equation, d =where d is

the distance between the system and target object, and c is the speed of light. The fitting parameters (A and B) and  $\Delta G$  can be experimentally determined.

The waveforms measured experimentally using the neuromorphic time-of-flight (ToF) system, for detecting objects at varying distances (40, 25, and 10 cm from left to right), are presented in Figure 3a. To compensate for the time delay caused by the parasitic capacitance and stray inductance of the system, an intentional spike delay was applied in the NLOS experiment. For neuromorphic ToF ranging and NLOS detection, a retro-reflective object with a metal-coated diameter of 5 cm and 0.9 reflectivity was used. According to the neuromorphic ToF learning rule, the conductance transition increases when the distance between the sensor and object decreases, leading to a higher peak potentiation. However, distance-dependent attenuation of the reflected optical signal also affects the conductance transition. We thus tested the feasibility of the neuromorphic ToF system using a presynaptic spike with different firing timings but with an identical amplitude and a fixed postsynaptic spike (Figure 3b). This approach was made possible through compact circuit design and post signal processing algorithms. 17,18 The peak potential of the programming signal decreased from 1.25 to 1 V when the temporal superposition between the presynaptic and postsynaptic spikes was reduced by 2 ns. This result confirmed that the difference between the firing timings of the presynaptic and postsynaptic spikes led to a tunable programming signal for the artificial synapses.

Finally, a neuromorphic ToF system is used for NLOS detection using a time gated STDP learning rule. This was achieved by overlapping the reference electrical signal and spike signal received after multiple reflections from the hidden target object and scattering wall, as shown in Figure 4a. The APD received two optical signals (Reflection 1 and Reflection 2), which originates from the wall and the target object, respectively. The time gated neuromorphic ToF system allowed only the signal reflected from the object to be coupled with the presynaptic spike to program the memristor. This was achieved by applying a presynaptic spike after the first strong reflection signal was received without forming highly superposed peaks. Thus, the presynaptic spike was coupled only with the signal reflected from the object, when the hidden object was in the scanning region. As expected, no second postsynaptic spike was generated unless the object existed in the scanning region. Figure 4b shows the simulated results of NLOS ray tracing using a two-dimensional model with geometrical optics (GOP). In this simulation, the target object was located at three angular positions (10°, 20°, and 30°), and the second peak was generated only when the object was in the corresponding angular position. Therefore, the second spike was coupled with the presynaptic spike to program the memristors.

We also conducted an experimental demonstration of the neuromorphic ToF-based NLOS detection, as illustrated in Figure 4c. The target object was positioned 48 cm from the center of the wall and rotated at an angular position of  $10^\circ$  to  $30^\circ$ . The laser source and receiver were co-rotated horizontally to detect the target objects located at different positions ( $10^\circ$ ,  $20^\circ$ , and  $30^\circ$  from the wall). Electrical input with an amplitude of 0.7 V and a pulse width of 30 ns was utilized as presynaptic spikes. The neuromorphic ToF system rotates to select one position ( $10^\circ$ ,  $20^\circ$ , or  $30^\circ$ ), and the target object is detected when the scanning direction matches that of the object. The

second peak in Figure 4c represents the signal reflected from the NLOS object, which was coupled to the memristor via the STDP learning rule in the neuromorphic ToF system. The first postsynaptic spike was time gated with an asynchronous postsynaptic spike to prevent programming through direct reflection from the wall. Therefore, only the NLOS signal (second peak) is coupled with the presynaptic spike, as shown in Figure 4c. When the NLOS optical scan is applied to an object located at the target angle, a superimposed spiking signal is applied to the memristor for programming, which represents the NLOS detection, as shown in Figure 4d. The superposed spiking power was calculated by squared voltage signals, multiplied by the average value of the HRS memristor of 7.287 k $\Omega$ , and integrated by time. Combined with this technique, the localization of the two angular bases in the polar coordinate can be carried out by a 2-axis steering system such as double axis MEMS mirrors. 16,19 Further practical implementation is also viable by using an APD array that can scan multiple spots in a single laser shot, so that the entire scanning time can be significantly reduced.<sup>20</sup> Integration with multiple focusing lenses and intensity-thresholding components, including comparator, amplifier, and filter circuits, <sup>21</sup> can alleviate target reflectivity and accurate detection timing issues, respectively. Moreover, digital and analog co-designed integrated circuits can offer practical solutions for addressing distance-related attenuation by using automatic gain modulation through digital logics for different distances and employing the signal regulation of the postsynaptic spike through an analog regulation circuit.<sup>22</sup>

The distance-dependent attenuation issue in the proposed system, similarly in LiDAR systems, is influenced by the ambient environment, target reflectivity, and distance. One effective way to address the ambient light effect is to use a near-infrared (NIR) light source, which can propagate robustly through the air. Neuromorphic ToF ranging and NLOS detection can be further improved by minimizing the parasitic parameters through system-on-chip structures and by using faster switching artificial synapses, such as ferroelectric, 8,23,24 spin-torque, 25,26 and phase-change devices. 27-29

In conclusion, we successfully demonstrated NLOS detection using a neuromorphic ToF method. HfO2 memristors were employed for neuromorphic ToF ranging via nanoscale sandwiching spikes, which exhibited an analog conductance transition via a pulse train. The coupling between presynaptic and postsynaptic spikes, electrical turn-on signals, and multiple-reflected optical signals enabled the NLOS detection via neuromorphic ToF. The presynaptic and second postsynaptic spikes were coupled when the target object was in the same direction as the scanning direction, resulting in high programming power for the memristors. The proposed neuromorphic NLOS detection features the processing of detection information in the memristor medium, thereby minimizing the need for additional signal processing algorithms and circuitry required for 3D ranging. We believe that neuromorphic ToF-based NLOS detection can provide a simplified and miniaturized 3D vision computing platform with potential applications in various engineering fields, such as automotive navigation,  $^{30-32}_{36-38}$  machine learning,  $^{9,33-35}_{9,33-35}$  and biomedical engineering.

### METHODS

**Device Fabrication.** The polyimide substrate was annealed at 200 °C for 30 min to prevent thermal expansion during the

fabrication process. The first 100 nm  ${\rm Al_2O_3}$  buffer layer was deposited via atomic layer deposition (ALD) at 200 °C, followed by e-beam evaporation of a 3/25-nm-thick Ti/Pt bottom electrode. A HfO<sub>2</sub> medium (5 nm) was deposited using ALD at 200 °C, and a Ta top electrode (55 mm²) of 50 nm thickness was deposited using DC magnetron sputtering.

Ray Tracing. The COMSOL Multiphysics software was used to simulate NLOS ray tracing. The refractive index of the object was 1.46, the maximum number of secondary rays was set to 500, and a wavelength of 660 nm was used to determine the ray properties. The cone angle of the beam emitted from the inlet was 18°. The object in this simulation was an ellipse with major and a minor axis of 22 and 4 cm, respectively. A scattered-reflection surface was used to determine the surface properties of the object. A-ray detector was used to count the photons passing through the detection area. The laser and detector were located at 10°, 20°, and 30° with respect to the center of the horizontally oriented rectangle. At these angles, the objects were placed 40 cm from the rectangular barrier and 27.5 cm above the horizontally oriented rectangle.

#### ASSOCIATED CONTENT

# **Data Availability Statement**

The data related to the figures and other findings of this study are available from the corresponding author upon request.

# AUTHOR INFORMATION

## **Corresponding Authors**

Junseok Heo — Department of Electrical and Computer Engineering, Ajou University, Suwon 16499, South Korea; orcid.org/0000-0002-8125-6141; Email: jsheo@ajou.ac.kr

Kyusang Lee − Department of Electrical and Computer Engineering and Department of Material Science and Engineering, University of Virginia, Charlottesville, Virginia 22904, United States; orcid.org/0000-0001-7123-3395; Email: kl6ut@virginia.edu

#### **Authors**

Minseong Park — Department of Electrical and Computer Engineering, University of Virginia, Charlottesville, Virginia 22904, United States

Yuan Yuan – Department of Electrical and Computer Engineering, University of Virginia, Charlottesville, Virginia 22904, United States

**Yongmin Baek** – Department of Electrical and Computer Engineering, University of Virginia, Charlottesville, Virginia 22904, United States

Byungjoon Bae – Department of Electrical and Computer Engineering, University of Virginia, Charlottesville, Virginia 22904, United States

Bo-In Park – Research Laboratory of Electronics and Department of Mechanical Engineering, Massachusetts Institute of Technology, Cambridge, Massachusetts 02139-4307, United States

Young Hoon Kim — Department of Electrical and Computer Engineering, Ajou University, Suwon 16499, South Korea Nicholas Lin — Department of Computer Science, University of Virginia, Charlottesville, Virginia 22904, United States

Complete contact information is available at: https://pubs.acs.org/10.1021/acsphotonics.3c00448

#### **Funding**

This study was funded by the National Science Foundation (NSF) (Grant No. 1942868) and the Industrial Strategic Technology Development Program (20014247) funded by the Ministry of Trade, Industry and Energy (MOTIE, Korea).

#### Notes

The authors declare no competing financial interest.

### ACKNOWLEDGMENTS

We acknowledge support for characterization from Prof. Joe C. Campbell.

# REFERENCES

- (1) Hebb, D. O. The Organization of Behavior: A Neuropsychological Theory, vol 50, 2018; pp 0–1.
- (2) Prezioso, M.; Merrikh Bayat, F.; Hoskins, B.; Likharev, K.; Strukov, D. Self-Adaptive Spike-Time-Dependent Plasticity of Metal-Oxide Memristors. *Sci. Rep.* **2016**, *6*, 21331.
- (3) Panwar, N.; Rajendran, B.; Ganguly, U. Arbitrary Spike Time Dependent Plasticity (STDP) in memristor by analog waveform engineering. *IEEE Electron Device Lett.* **2017**, *38*, 740–743.
- (4) Roe, D. G.; et al. Humanlike spontaneous motion coordination of robotic fingers through spatial multi-input spike signal multiplexing. *Nat. Commun.* **2023**, *14*, 5.
- (5) Kumar, S.; Wang, X.; Strachan, J. P.; Yang, Y.; Lu, W. D. Dynamical memristors for higher-complexity neuromorphic computing. *Nat. Rev. Mater.* **2022**, *7*, 575.
- (6) Wang, Z.; et al. Resistive switching materials for information processing. *Nat. Rev. Mater.* **2020**, *5*, 173–195.
- (7) Deng, X.; et al. A flexible mott synaptic transistor for nociceptor simulation and neuromorphic computing. *Adv. Funct. Mater.* **2021**, *31*, No. 2101099.
- (8) Yang, J. Y.; et al. Reconfigurable Radio-Frequency High-Electron Mobility Transistors via Ferroelectric-Based Gallium Nitride Heterostructure. *Adv. Electron. Mater.* **2022**, *8*, No. 2101406.
- (9) Lee, D.; et al. In-sensor image memorization and encoding via optical neurons for bio-stimulus domain reduction toward visual cognitive processing. *Nat. Commun.* **2022**, *13*, 5223.
- (10) Park, M.; et al. Neuron-Inspired Time-of-Flight Sensing via Spike-Timing-Dependent Plasticity of Artificial Synapses. *Adv. Intell. Syst.* **2022**, *4*, 2100159.
- (11) Park, M.; et al. Hetero-integration enables fast switching time-of-flight sensors for light detection and ranging. *Sci. Rep.* **2020**, *10*, 2764.
- (12) Jiang, Y.; Karpf, S.; Jalali, B. Time-stretch LiDAR as a spectrally scanned time-of-flight ranging camera. *Nat. Photonics* **2020**, *14*, 14–18.
- (13) Palaniappan, A. R.; Siek, L. A 0.6 V, 1.74 ps resolution capacitively boosted time-to-digital converter in 180 nm CMOS. *Proceedings IEEE International Symposium on Circuits and Systems*, 2019; pp 2019–2022.
- (14) Hassan, O. H., Rashed, K. R., Hussien, F. A., Aboudina, M. M. A 4-bit 2ps resolution time-to-digital converter utilizing multi-path delay line for ADPLL. *Proceedings of the International Conference on Microelectronics, ICM*, 2019; pp 210–213.
- (15) Ximenes, A. R.; et al. A 256×256 45/65nm 3D-stacked SPAD-based direct TOF image sensor for LiDAR applications with optical polar modulation for up to 18.6dB interference suppression. In 2018 IEEE International Solid State Circuits Conference (ISSCC), 2018; pp 96–98
- (16) Otoole, M.; Lindell, D. B.; Wetzstein, G. Confocal non-line-of-sight imaging based on the light-cone transform. *Nature* **2018**, *555*, 338–341.
- (17) Glaser, J. How GaN power transistors drive high-performance Lidar: Generating ultrafast pulsed power with GaN FETs. *IEEE Power Electron. Mag.* **2017**, *4*, 25–35.

- (18) Richter, K.; Maas, H.-G.; Westfeld, P.; Weiß, R. An approach to determining turbidity and correcting for signal attenuation in airborne lidar bathymetry. *PFG* **2017**, *85*, 31–40.
- (19) Yamashita, H.; et al. Dual-axis hybrid-MEMS mirror having Si and polymer hinges for large-area 2D raster scan. In 2014 International Conference on Optical MEMS and Nanophotonics; IEEE, 2014; pp 167–168.
- (20) Tan, C.; et al. Long-Range Daytime 3D Imaging Lidar With Short Acquisition Time Based on  $64 \times 64$  Gm-APD Array. *IEEE Photonics J.* **2022**, *14*, 1–7.
- (21) Chevrier, M.; Campanella, G. How to build a LIDAR system with a time-to-digital converter. *Analog Appl. J.* **2017**, 1–6.
- (22) Zhang, Y.; An, Y. Computational three-dimensional imaging method of compressive LIDAR system with gain modulation. In LIDAR Imaging Detection and Target Recognition 2017; Lv, Y.; et al., Ed.; SPIE, 2017, vol 10605; pp 44–48.
- (23) Ryu, H.; Wu, H.; Rao, F.; Zhu, W. Ferroelectric Tunneling Junctions Based on Aluminum Oxide/ Zirconium-Doped Hafnium Oxide for Neuromorphic Computing. Sci. Rep. 2019, 9, 20383.
- (24) Ma, C.; et al. Sub-nanosecond memristor based on ferroelectric tunnel junction. *Nat. Commun.* **2020**, *11*, 1439.
- (25) Tokura, Y.; Seki, S.; Nagaosa, N. Multiferroics of spin origin. Rep. Prog. Phys. 2014, 77, 76501.
- (26) Manipatruni, S.; et al. Scalable energy-efficient magnetoelectric spin—orbit logic. *Nature* **2019**, *565*, 35–42.
- (27) Wright, C. D.; Liu, Y.; Kohary, K. I.; Aziz, M. M.; Hicken, R. J. Arithmetic and biologically-inspired computing using phase-change materials. *Adv. Mater.* **2011**, *23*, 3408–3413.
- (28) Burr, G. W.; et al. Experimental demonstration and tolerancing of a large-scale neural network (165,000 synapses), using phase-change memory as the synaptic weight element. 2014 IEEE International Electron Devices Meeting vol XX, 2014; pp 29.5.1–29.5.4.
- (29) Kim, S.; et al. NVM neuromorphic core with 64k-cell (256-by-256) phase change memory synaptic array with on-chip neuron circuits for continuous in-situ learning. *Technical Digest International Electron Devices Meeting, IEDM*, 2016; pp 17.1.1–17.1.4.
- (30) Hinz, G.; et al. Online multi-object tracking-by-clustering for intelligent transportation system with neuromorphic vision sensor. In *Joint German/Austrian Conference on Artificial Intelligence (Künstliche Intelligenz)*; Springer, 2017; pp 142–154.
- (31) Lamoureux, A.; Lee, K.; Shlian, M.; Forrest, S. R.; Shtein, M. Dynamic kirigami structures for integrated solar tracking. *Nat. Commun.* **2015**, *6*, 8092.
- (32) Lee, K.; Lee, J.; Mazor, B. A.; Forrest, S. R. Transforming the cost of solar-to-electrical energy conversion: Integrating thin-film GaAs solar cells with non-tracking mini-concentrators. *Light: Sci. Appl.* **2015**, *4*, e288–e288.
- (33) Bae, B.; Park, M.; Lee, D.; Sim, I.; Lee, K. Hetero-Integrated InGaAs Photodiode and Oxide Memristor-Based Artificial Optical Nerve for In-Sensor NIR Image Processing. *Adv. Opt. Mater.* **2023**, *11*, No. 2201905.
- (34) Wang, T.; et al. Reconfigurable optoelectronic memristor for insensor computing applications. *Nano Energy* **2021**, *89*, No. 106291.
- (35) Zhou, F.; Chai, Y. Near-sensor and in-sensor computing. *Nat. Electron.* **2020**, *3*, 664–671.
- (36) Ciesla, C. M. et al. Biomedical applications of terahertz pulse imaging. *Commercial and Biomedical Applications of Ultrafast Lasers II*, 2000, vol 3934; p 73.
- (37) El-Hajj, C.; Kyriacou, P. A. A review of machine learning techniques in photoplethysmography for the non-invasive cuff-less measurement of blood pressure. *Biomed. Signal Process. Control* **2020**, 58, No. 101870.
- (38) Tanveer, M. S.; Hasan, M. K. Cuffless blood pressure estimation from electrocardiogram and photoplethysmogram using waveform based ANN-LSTM network. *Biomed. Signal Process. Control* **2019**, *51*, 382–392.